Analysis of CO_2 mole fraction data: first evidence of large-scale changes in CO_2 uptake at high northern latitudes

J. M. Barlow[1], P. I. Palmer[1], L. M. Bruhwiler[2], and P. Tans[2]

[1]School of GeoSciences, University of Edinburgh, UK
[2]US National Oceanic and Atmospheric Administration, Global Monitoring Division, Earth System Research Laboratory, Boulder, Colorado, USA

Correspondence to: J. M. Barlow
(jbarlow@staffmail.ed.ac.uk)

Abstract. Atmospheric variations of carbon dioxide (CO_2) mole fraction reflect changes in atmospheric transport and regional patterns of surface emission and uptake. We report new estimates for changes in the phase and amplitude of observed high northern latitude CO_2 seasonal variations, indicative of biospheric changes, by spectrally decomposing multi-decadal records of surface CO_2

5   mole fraction using a wavelet transform to isolate the changes in the observed seasonal cycle. We also perform similar analysis of the first time derivative of CO_2 mole fraction, $\Delta_t CO_2$, that is a crude proxy for changes in CO_2 flux. Using numerical experiments, we quantify the aliasing error associated with independently identifying trends in phase and peak uptake and release to be 10–25%, with the smallest biases in phase associated with the analysis of $\Delta_t CO_2$. We report our analysis from

10   Barrow, Alaska (BRW) during 1973–2013, which is representative of the broader Arctic region. We determine an amplitude trend of 0.09±0.02 ppm/yr, which is consistent with previous work. Using $\Delta_t CO_2$ we determine estimates for the timing of the onset of net uptake and release of CO_2 of -0.14±0.14 and -0.25±0.08) days/yr, respectively, and a corresponding uptake period of -0.11±0.16 days/yr, which are significantly different to previously reported estimates. We find that the wavelet

15   transform method has significant skill in characterizing changes in the peak uptake and release. We find a trend of 0.65±0.34% (p<0.01) and 0.42±0.34% (p<0.05) for rates of peak uptake and release, respectively. Our analysis does not provide direct evidence about the balance between uptake and release of carbon, but changes in the peak uptake and release together with an invariant growing period length provides indirect evidence that high northern latitude ecosystems are progressively

20   taking up more carbon.

1 Introduction

Combustion of fossil fuel and cement production represent the dominant annual source of atmospheric CO_2 variation. There is also a minor source from the combustion of biomass and a diffuse source from the emissions and oxidation of reduced carbon (Suntharalingam et al., 2005). On an annual basis approximately 50% of those emissions remain in the atmosphere with the remainder taken up by the land and ocean biosphere (Ballantyne et al., 2012). Regional changes to the net biospheric flux of CO_2, and consequent changes in atmospheric CO_2, are due to a) spatial and temporal changes in climate, b) different responses of vegetation to these changes in climate, and c) other factors that may dominate over climate, e.g., nutrient availability. A recent study, building on extensive literature, have reported substantial increases in the amplitude of the seasonal exchange of CO_2 since the 1950s, particularly at mid to high northern latitudes (Graven et al., 2013). Here, we use the wavelet transform to isolate changes in the CO_2 seasonal cycle, revealing new insights about the growth rate, and changes in the amplitude and phase of CO_2 associated with the growing season.

Analysis of atmospheric measurements of CO_2 to describe changes in the seasonal cycle has been explored in previous studies. These studies have typically employed curve fitting techniques (e.g. Bacastow et al. (1985), Thompson et al. (1986), Keeling et al. (1996), Piao et al. (2008), Barichivich et al. (2012) and Barichivich et al. (2013)) or filtering methods such as complex demodulation (Thompson and Clark (2008) and Thompson (2011)). We apply a wavelet transform (Torrence and Compo, 1998), which uses a pre-defined wave-like oscillation that is non-continuous in time or space to decompose a time series into time-frequency space, allowing us to investigate the dominant modes of variability and how they change with time. The wavelet transform can decompose CO_2 time series into its seasonal cycle and long-term trend while retaining information about phase and amplitude (Torrence and Compo, 1998). Not accounting for these simultaneous changes can compromise the isolation of frequencies that contribute to the seasonal cycle and potentially leads to erroneous conclusions about changes in the CO_2 seasonal cycle. We show through extensive analysis of synthetic time series of the first time derivative of CO_2, $\Delta_t CO_2$, that the wavelet transform can better separate changes in the phase and amplitude of the seasonal cycle than analysis of CO_2 mole fraction. We also show that the wavelet can also faithfully reproduce changes in the rates of peak uptake and peak release of CO_2, allowing us to understand observed changes in the amplitude of the seasonal cycle.

In the next section we describe measurements of CO_2 mole fraction, $\delta^{13}C$, surface temperature, and vegetation indices; and the approach we have employed to impute these data. In section 3, we describe the wavelet transform that we use to spectrally decompose these data, including a characterisation of the aliasing error associated with independent inference of changes in phase, amplitude and the magnitude and timing of the peak uptake and release of CO_2. In section 4, we present our analysis of CO_2 growth rates, changes in the phase and amplitude of the CO_2 seasonal cycle. We conclude our paper in section 5.

2

2 Data

2.1 CO$_2$ mole fraction data

60 Figure 1 shows the high latitude sites from the NOAA Cooperative Global Air Sampling Network (Dlugokencky et al., 2014), which include at least 15 years of CO$_2$ mole fraction data. We focus on high northern latitude sites where a) transport is relatively zonal so that observed variations of CO$_2$ are due to CO$_2$ fluxes at the same latitude band (Figure 2) and b) contributions to observed CO$_2$ from continents at these latitudes are approximately equal. We report our CO$_2$ analysis for BRW

65 because it is generally considered to be representative of the broader Arctic region, and report our analysis from other sites in an appendix.

Twin air samples are collected weekly at the sites and analysed for CO$_2$ at NOAA ESRL in Boulder, Colorado using a non-dispersive infrared analyser. These data are suitable to study variations on weekly and longer timescales. Single measurement uncertainties are calculated based on the

70 ability to propagate the World Meteorological Organisation (WMO) XCO$_2$ scale to working standards (±0.03 ppm, Zhao and Tans (2006)), the analytical repeatability of the analysers for a sample measurement (±0.03 ppm), and the agreement between pairs of samples collected simultaneously (±0.1 ppm across the entire sampling network). The sum of these uncertainties is negligible in comparison to the magnitude of CO$_2$ variability observed at northern high latitudes.

2.2 Imputation of mole fraction data

The wavelet transform method (described below) requires a continuous time series regularly spaced in time. To fill a missing value in a time series we take it from a local temporally mean seasonal cycle (3 years either side of the missing value) and a value from a deseasonalised reference time series (Figure 3), accounting for large-scale anomalies in the growth rate. Any remaining missing

80 datapoints are extracted from a piecewise cubic spline curve fit. Parts of the time series that contain significant sections of missing data are likely to be unreliable, however prolonged periods are rare and we find that isolated missing data points do not significantly impact the determination of long term trends in the phase and amplitude.

Figure 4 shows an example of our imputation approach using the CO$_2$ mole fraction and δ^{13}C

85 time series from Cold Bay Alaska.

2.3 δ^{13}CO$_2$ data

We also use measurements of δ^{13}C that are colocated with the CO$_2$ mole fraction data. These help us attribute observed changes of CO$_2$ mole fraction to land biospheric uptake and release. The ratio

3

δ^{13}C is defined as:

$$\delta^{13}\text{C} = \left[\frac{\left[\frac{^{13}\text{C}}{^{12}\text{C}} \right]_{sample}}{\left[\frac{^{13}\text{C}}{^{12}\text{C}} \right]_{standard}} - 1 \right] \times 1000, \tag{1}$$

where $\left[\frac{^{13}\text{C}}{^{12}\text{C}} \right]_{sample}$ is the ratio of ^{13}C to ^{12}C within the sample, and $\left[\frac{^{13}\text{C}}{^{12}\text{C}} \right]_{sample}$ is the ratio of ^{13}C to ^{12}C in a standard (a substance with a known, unchanging ^{13}C to ^{12}C ratio). Individual measurements of ^{12}C and ^{13}C are determined by isolating the CO_2 in a subsample of air from each flask and using a mass spectrometer to determine the isotopic composition.

2.4 Ancillary data

We use the University of East Anglia Climate Research Unit TS3.10 land temperature dataset (Harris et al., 2013) to help interpret observed variations in the CO_2 time series. This data has a 0.5×0.5 degree spatial resolution and monthly time resolution.

To investigate large-scale vegetation change, we use the Global Inventory Modeling and Mapping Studies normalized difference vegetation index (GIMMS NDVI3g) dataset derived from the NOAA Advanced Very High Resolution Radiometer (AVHRR) (Pinzon et al., 2005; Tucker et al., 2005). NDVI, calculated from the visible and near-infrared light reflected by vegetation, is strongly correlated with photosynthetic activity in vegetation canopies; although we acknowledge photosynthesis may not accompany greenness a) at high latitudes when water is frozen and b) during drought when stomates are mostly closed. These NDVI data have a spatial resolution of approximately 8 km and a twice monthly temporal resolution from 1982 to the end of 2006. The dataset has been corrected for calibration, viewing geometry, volcanic aerosols, and other effects not related to vegetation change. We remove pixels that have a time series mean NDVI value of <0.1, to ensure that areas with bare or sparse vegetation are not included in spatial averages.

3 Wavelet transform

We use a wavelet transform to spectrally decompose the observed CO_2 variations into individual frequency bands that can be attributed to the responsible biological and physical processes.

In general a wavelet transform W_n uses a wavelet function ψ_0, a pre-defined wave-like oscillation that is non-continuous in time or space, to decompose a time series into time-frequency space, allowing us to investigate the dominant modes of variability and how they change with time. This improves on the Fourier transform that determines frequency information using sine and cosine functions.

The wavelet transform of a time series x_n is defined as

$$W_n(s) = \sum_{k=0}^{N-1} \hat{x}_k \hat{\psi} * (s\omega_k) e^{i\omega_k n\delta t}, \tag{2}$$

4

where $\hat{x}_k$ is the discrete Fourier transform of x_n, N is the number of points in the time series, $k=0...N-1$ is the frequency index and $\hat{\psi}*(s\omega_k)$ is the complex conjugate of the Fourier transform of a normalized, scaled and translated version of $\psi_0(\eta)$, where s is the scale and ω_k is the angular frequency. We use the Morlet wavelet (Torrence and Compo, 1998), a plane wave modulated by a gaussian envelope:

$$\psi_0(\eta) = \pi^{-1/4} e^{i\omega_0 \eta} e^{-\eta^2/2}, \tag{3}$$

where ω_0 is the nondimensional frequency and η is the non-dimensional time-parameter. We chose the Morlet wavelet because it is nonorthogonal, which is an attractive property for the analysis of smooth and continuous variations such as those exhibited by CO_2 mole fraction time series. The wavelet is comprised of a real and imaginary part, providing information about amplitude and phase, respectively.

We can recover the original time series from wavelet space using the corresponding inverse transform (Torrence and Compo, 1998) and summing over all frequencies from the real part of the wavelet transform or a subset of frequencies if we are interested in isolating signals:

$$\hat{W}_n = \frac{\delta j \delta t^{1/2}}{C_\delta \psi_0(0)} \sum_{j=0}^{J} \frac{\Re\{W_n(s_j)\}}{s_j^{1/2}}, \tag{4}$$

where $\psi_0(0)$ removes the energy scaling and $s_j^{1/2}$ converts the wavelet transform to an energy density. C_δ and $\psi_0(0)$ are constants determined for the specific wavelet function.

To minimize edge effects associated with the Fourier transform, we add synthetic data to pad the start and end of the time series. For our calculation we repeat the first (last) data point backward (forward), accounting for a growth rate based on following (preceding) years. We also "zero pad" the time series so that the number of points used is an integral power of two, which further reduces edge effects and speeds up the transform. The addition of the padded data allows us to use the edges of the time series by ensuring that there is negligible additional error introduced by edge effects, but uncertainty in the spectral decomposition is still likely to be largest at these points. The padded data at the edges of the time series are removed post wavelet decomposition and prior to analysis.

We quantify the numerical error associated with the wavelet transform by applying it to synthetic time series, which are representative of CO_2 time series with a prescribed trend. We find that the value for C_δ previously reported (Torrence and Compo, 1998) introduces a small trend in the original minus reconstructed residual, and find that C_δ=0.7784 results in a much smaller, unbiased residual with a typical value <0.05ppm for monthly data and <0.002ppm for weekly data (not shown). Table 1 shows the wavelet parameter values that we used in our analysis.

Additional uncertainties may arise in the long term trend and detrended seasonal cycle as a result of spectral power being assigned to the incorrect frequency band. This could, for example, result in concentration changes caused by anthropogenic emissions being misattributed to the natural (seasonal) cycle of CO_2, and vice versa. However, this is a common weakness of any method used to

155 decompose such time series.

We find that for atmospheric CO_2, the wavelet power spectrum peaks at periods (reciprocal of frequency) of 6 and 12 months (Appendix A), with a spread across these periods associated with the sampling of the data. To study annual changes in phase and amplitude we retain period of 3 to 18 months, and assume that periods longer than 18 months are indicative of the growth rate and periods

160 shorter than three months are due to local/regional sources that are unrelated to the seasonal cycle (described using an example in Appendix A).

4 Results

4.1 Growth rates

Figure 5 shows how the decadal atmospheric growth rate has changed from the 1980 to 2009 as

165 a function of latitude. We find that in the 1980s and 1990s the growth rates are approximately the same in the southern hemisphere, but diverge further north. The 1980-1989 growth rate rises sharply towards the northern high latitudes while there is a dip in the 1990–1999 in the same latitude band. We anticipate that this is partially due to the collapse of the Soviet Union but also due to changes in biospheric uptake in the northern hemisphere. It should be noted that the number of CO_2

170 monitoring stations in the 1980s is considerably more sparse. The 2000-2009 decadal mean growth rate is significantly higher than both of the previous decades by ~ 0.35ppm yr^{-1} and rises from the southern hemisphere to mid-latitude northern hemisphere before dropping off again in the northern high latitudes. We find that our annual CO_2 growth rates at Mauna Loa are within a fraction of a percent of NOAA values.

175 By subtracting anthropogenic fossil fuel emission estimates from the atmospheric CO_2 signal (Table 2) we can effectively isolate uptake by the oceans and terrestrial biosphere, acknowledging the uncertainties associated with the emission estimates and that we have not accounted for land use change emissions. The residual growth rate is negative, as expected (Ballantyne et al., 2012). We find that during the 1980s the net annual uptake by the terrestrial biosphere and ocean was

180 typically -1.03$\pm$0.11 ppm/year. This rate increases dramatically in the 1990s to approximately -1.54$\pm$0.06 ppm/year and to -1.89$\pm$0.08 ppm/year in 2000s. This change in the growth rate supports the notion that the natural component of the carbon cycle is increasing the amount of carbon it takes up in response to the amount of carbon present in the atmosphere, although the last two decades show a smaller increase in net annual uptake. This apparent equilibrium state results in an approxi-

185 mate mean airborne fraction of 55.8$\pm$18.2% (including only fossil fuel) and 44.1$\pm$14.4% (including fossil fuel and land use change), consistent with previous work (Gloor et al., 2010). For the purpose of the following calculations we have removed the annual growth rate from the observed CO_2 concentrations, following the method described in Appendix A.

4.2 Phase and amplitude analysis

We use several metrics to interpret the detrended CO_2 mole fraction time series: the seasonal amplitude and zero-crossing points for CO_2 and for the first differential of CO_2 ($\Delta_t CO_2$), and the rate of change of peak uptake (PU) and peak release (PR) for $\Delta_t CO_2$. We use $\Delta_t CO_2$ mole fraction data as a crude proxy for the responsible net flux of CO_2. As we discuss below and report in Appendix B, analysis of $\Delta_t CO_2$ leads to less biased estimates for trends in the PU and PR and phase of the CO_2 seasonal cycle. As part of our analysis we report 95% confidence intervals, the Pearson correlation coefficient r, and p-values that denote the probability of reproducing a result by chance; for practical purposes p-values >0.05 represent a result that is not significant.

Practical definitions and theoretical calculations

Figure 6 shows, using example data from BRW, how the detrended CO_2 and $\Delta_t CO_2$ variations are related. The amplitude of the seasonal cycle, defined as the peak-to-peak difference (maxima minus minima) of the seasonal CO_2 mole fraction time series, has been used in previous studies as a measure of biological activity (e.g., Keeling et al. (1996); Graven et al. (2013)). In theory, this metric alone cannot tell us whether net uptake or release is responsible for observed variations, so it is typically used as an indicator of overall net seasonal carbon exchange, although recent work has shown that the intense period of uptake at high northern latitudes contributes more to the seasonal amplitude than the longer period of emission.

Based on $\Delta_t CO_2$ we define three periods during an annual cycle: 1) an uptake period when $\Delta_t CO_2 < 0$ and there is a net negative CO_2 flux to the atmosphere (photosynthesis is higher than respiration); 2) a release period when $\Delta_t CO_2 > 0$ and there is a net source of CO_2 to the atmosphere; and 3) a dormant period, defined between the latter half of winter and the start of the next uptake period, when plant activity is very low due to frozen ground so that $\Delta_t CO_2$ is typically small (but non-zero due to transport of CO_2 from the lower latitudes). Zero-crossing points (ZCP) refer to times when the detrended seasonal cycle is equal to zero (e.g., Piao et al. (2008)). For a seasonal cycle there is a downward and upward ZCP (DZCP and UZCP, respectively) within one year. The DZCP is a proxy for northern hemisphere spring onset of CO_2 uptake, and similarly the UZCP is a proxy for the onset of net carbon release in northern hemisphere autumn. $\Delta_t CO_2$ phase thresholds are analogous to the CO_2 mole fraction ZCPs that look at the timing of when vegetation becomes a net CO_2 source or sink, but also take into account that observed variations can introduce local maxima/minima particularly associated with the DZCP. The $\Delta_t CO_2$ DZCP is particularly difficult to determine using the BRW seasonal cycle because small mole fraction variations during the dormant period (which has a near-zero flux) are sufficient to bring $\Delta_t CO_2$ below zero before the carbon uptake period associated with the growing season. To address this we have tested a number of phase thresholds which represent the timing of when certain thresholds in $\Delta_t CO_2$ are reached (e.g. 25%

of PU). We find that using the 25% of PU is a more robust indicator of spring timing rather than the DZCP. In contrast, the $\Delta_t CO_2$ UZCP is well defined and trivial to calculate. We define a carbon uptake period (CUP), which is the difference between the autumn and spring phase metrics defined above. PU and PR refer to the minima and maxima of the flux time series, respectively. As we show below using theoretical calculations these peak values are related to annual release and uptake.

The ability of the wavelet transform to isolate changes in the phase and amplitude of the seasonal cycle with fidelity is critical for our analysis. We use Monte Carlo numerical experiments to characterize the aliasing errors associated with independently identifying changes in phase and amplitude that can result in the misinterpretation of these data and/or underestimation of uncertainties (Appendix B). These errors are not unique to the wavelet transform but to our knowledge they have not been reported by previous studies focused on time series analysis of CO_2 mole fractions. We generally find that analysis of $\Delta_t CO_2$ produces more reliable and less biased estimates than CO_2 trend estimation of either phase with an estimated 25% systematic aliasing error (Appendix B). Unless explicitly stated all subsequent results will refer to our analysis $\Delta_t CO_2$. We also find that the wavelet transform can capture at least 80% of independent trends in the PU and PR of the $\Delta_t CO_2$ seasonal cycle, which has not been reported previously and allows us to study changes in characteristics more closely related to annual changes in biological release and uptake of CO_2 (Appendix B).

Analysis of NOAA CO_2 mole fraction data

Figure 7 shows that changes in downward and upward phase BRW are -0.14 days/yr (p<0.05) and -0.25 days/yr (p<0.01), respectively, with a corresponding CUP change of -0.11 days/yr (p>0.1); the analysis of the other study sites is shown in Appendix C. We find no evidence using phase changes of CO_2 or $\Delta_t CO_2$ for a significant change in CUP throughout the measurement period. Analysis of CO_2 shows a much tighter coupling between the timing of the downward and upward phases with values of -0.20 days/yr (p<0.01) and -0.18 days/yr (p<0.05) respectively. This results in a more conserved CUP, with a trend of 0.02 days/yr (p>0.1), which is consistent with the ecosystem having an intrinsic uptake period (not shown). Recent work using changes in CO_2 has reported a change of -0.17 days/yr for the downward phase over a similar time period (Graven et al., 2013).

The concomitant observed changes in $\Delta_t CO_2$ and in $\delta^{13}C$ (Appendix D) supports the idea that observed CO_2 variations are primarily due to changes in the terrestrial biosphere. Analysis of surface temperature analyses and space-borne observations of NDVI also corroborate the downward phase change of $\Delta_t CO_2$ (Appendix D). We find the start of the thermal growing season (defined as the continuous period above 5°C, Appendix D) is advancing two (three) times faster at latitudes >45°N (>60°N), which agrees with previous studies (e.g., Barichivich et al. (2012)). However we find an anticorrelation of autumn phase changes with NDVI and temperature anomalies. The NDVI anomalies during summer have not significantly increased on large spatial scales over the measurement period (1982–2006) compared with spring and autumn anomalies. This suggests that the increase

8

in net exchange of carbon between vegetation and the atmosphere is likely a result of increased activity during spring and autumn but this not consistent with analyses of CO_2 time series that show more uptake uptake in spring and summer. A number of studies have linked increases in NDVI and subsequent carbon uptake with a CO_2 fertilisation effect (Lim et al., 2004; Kaufmann et al., 2008; Los, 2013)) which may also be partly responsible for the observed increases in carbon uptake. Our analysis of NDVI data shows that increases of vegetation greenness in spring and autumn have led to significant lengthening of the photosynthetic growing season over the measurement period, where autumn greening is changing in most regions at a greater rate than spring greening.

Observed changes in amplitude at BRW (0.09±0.02 ppm/yr) are consistent in percentage terms with previous work over the same time period (Graven et al., 2013). As mentioned above, using the wavelet transform to isolate the seasonal cycle we also have skill at attributing the changes in the peak-to-peak amplitude to corresponding changes in the rates of PU and PR (Appendix B). We find that the observed change in amplitude at BRW is due to an increase in PR (0.42±0.34 ppm/yr, p>0.05) and a larger increase in PU (0.65±0.34 ppm/yr, p<0.01). Figure 8 shows that statistically significant trends (p<0.05) in PU are observed at five of the seven high latitude sites (ALT, BRW, CBA, ICE and ZEP, SOM). In most of these cases, the change in PU is significantly larger than the change in PR, and we show that changes in amplitude are determined mainly by changes in uptake (Appendix C). Previous analysis of these data has shown that changes in atmospheric transport cannot explain changes in the amplitude (Graven et al., 2013).

5   Concluding remarks

We have used a wavelet transform to spectrally isolate changes in the seasonal cycle of atmospheric CO_2 mole fraction. The wavelet transform can simultaneously separate the long-term trend and seasonal cycle while retaining information about changes in amplitude and phase. We focused on high northern latitude sites where transport is a) relatively zonal so that observed variations are due to fluxes at the same latitude band, and b) contributions to sampled CO_2 from continents at these latitudes are approximately equal.

We found that the atmospheric growth rate of CO_2 at these sites are within a few percent of reported values from NOAA. Our growth rates show large decadal changes, as expected, and once the anthropogenic signature has been removed we find strong evidence of a natural biospheric signal that is responding to increasing atmospheric CO_2 concentrations. This results in a near-constant airborne CO_2 fraction of 55.8±18.2% (including only fossil fuel) and 44.1±14.4% (including fossil fuel and land use change), consistent with previous studies.

Using the detrended CO_2 time series (original data minus growth rate) we examined the change in phase and amplitude of the seasonal cycle. Using a series of synthetic experiments we showed that the wavelet transform approach of isolating the seasonal cycle retained our ability to observe

9

295   independent changes in phase and peak uptake and release. We also showed that using the first time derivative of CO_2, $\Delta_t CO_2$, resulted in smaller biases in the independent estimation of trends in phase, within 10–25% of the "true" values.

    We reported an increase in amplitude of 0.09±0.02 ppm/yr, consistent with previous studies, which can be crudely associated with an increase in biological activity. Using a series of Monte

300   Carlo experiments we showed that the isolated seasonal cycle was sufficiently robust that we can identify changes in the magnitude and timing of peak uptake and release. We showed that the increase in amplitude is due to increasing respiration (peak) and greater drawdown (trough) with the drawdown increasing at a significant and faster rate.

    We diagnosed phase changes using thresholds associated downward and upward zero crossing

305   points when the seasonal cycle of $\Delta_t CO_2$ is zero during the downward and upward phases, respectively. These phase thresholds take into account that observed $\Delta_t CO_2$ variations can introduce local maxima/minima particularly associated with the downward zero crossing point. To address this we use the threshold of 25% of peak uptake, which we find is a more robust indicator of spring timing. We reported changes in the downward and upward phase of -0.14±0.14 day/yr and -0.25±0.08

310   days/yr, respectively, and a corresponding revision of the uptake period of -0.11±0.16 days/yr. Given that we characterized the method used to determine the change in phase, including a measure of uncertainty, and showed that analyzing $\Delta_t CO_2$ produced less biased estimates for these changes we argue that our values are a more faithful depiction of the truth.

    Our analysis does not provide direct evidence about the balance between uptake and release of

315   carbon, but changes in the peak uptake and release together with an invariant growing period length provides indirect evidence that high northern latitude ecosystems are progressively taking up more carbon. Changes in atmospheric CO_2 mole fraction tell us only part of the underlying carbon cycle story in terms of how the underlying ecosystems are changing. Clearly, additional measurements and models needs to be applied for us to understand observed changes in atmospheric CO_2. A more

320   frequent inspection of these data using advanced statistical tools such as the wavelet transform also have a role to play.

Appendix A   Example of spectral decomposition

Figure 10 shows, as an example, the spectral decomposition of CO_2 mole fraction measurements at Mauna Loa. The wavelet transforms decomposes the 1-D time series into a 2-D power spectrum,

325   describing energy per unit time, as a function of frequency (the reciprocal of period) and time. The cone of influence is the boundary below which wavelet coefficients are most compromised by edge effects. We have padded the edges of the CO_2 time series with additional synthetic data so we are able to analyse the entire CO_2 time series (section 3). We find that most of the power is in the annual and semi-annual periods, as expected, but also peaks in power at period > 1 year but this

330 is likely a result of responses of the CO_2 growth rate to large scale climate variability, e.g., the El Niño-Southern Oscillation. This is supported by the global wavelet power spectra (integrated over all time). The interannual growth rate is determined by taking the value of the long term trend (periods > 18 months) on January 1st in one year, and subtracting the value from the previous year to leave the net change in concentration.

335 As discussed above, we use the spectrally decomposed dataset to interpret the observed variability of CO_2 mole fraction data. Figure 10 shows two example applications: 1) as a lowpass filter to deseasonalize the CO_2 data (removing periods < 18 months); and 2) the associated annual growth rate (ppm/year), which we find is within <0.1 ppm of the reported values from NOAA (not shown).

Appendix B   Error characterisation of phase and amplitude estimates

340 We use synthetic CO_2 time series data, defined with specific changes in amplitude and phase, to characterize aliasing errors due to application of the wavelet transform of CO_2 concentration data or its first time derivative ($\Delta_t CO_2$). Insights from this synthetic analysis are directly applied to our interpretation of NOAA mole fraction measurements in the main paper.

B1   Synthetic model framework

345 We use a simple box model based on the CO_2 mole fraction time series at Barrow, Alaska (BRW, Figure 11). BRW is the most suitable site for this purpose because is has a long time series and as it is representative of high latitude CO_2 in the Northern Hemisphere. We take the first time derivative of the detrended time series at BRW to get the "flux" time series. We then take the mean seasonal cycle of the CO_2 flux and adjust it so that in its initial state, the source and sink terms are balanced.

350 This cycle is then repeated for 40 years (equivalent to the timespan of the BRW data) and integrated to convert the flux to CO_2 concentration. For our experiments, described below, we introduce trends and variability to various aspects of $\Delta_t CO_2$ before integrating with respect to time to recover CO_2 mole fraction. Detrending is as as described in the main paper.

B2   Numerical Experiments

355 The starting point of our numerical experiments is the detrended time series of atmospheric CO_2 mole fraction. Our analysis here as it is in the main paper does not provide direct evidence about the balance between uptake and release of carbon. The detrending process results in a seasonal cycle that integrates to zero over a year, which can if not properly accounted for introduce false trends and variability in the seasonal cycle metrics. We combine the metrics defined above to provide indirect

360 evidence of trends in the carbon balance of the Northern Hemisphere.

The following three broad set of experiments are designed to identify the best metrics to describe changes in the contemporary cycle from detrended CO_2 mole fraction measurements. First, we

perturb the timing of spring or autumn by adding or subtracting a smooth gaussian curve with a flat top centered roughly about the onset of net uptake or release, and increase the magnitude of the curve each year to introduce a trend across the time series. Second, we perturb the magnitude of net uptake or net release by multiplying the uptake (negative $\Delta_t CO_2$) or release (positive $\Delta_t CO_2$) by some factor, and increase the factor each year to introduce a trend. Finally, we add year to year variability (or noise) to the time series to assess the ability of our spectral method to extract trends from the data. We compare each metric by calculating the percentage difference in trend from the input time series and the wavelet detrended time series.

Perturbing the timing of the spring and autumn phases

Figure 12 shows the results of our analysis of a time series for which we introduced a progressively earlier onset of net CO_2 uptake of 0.50 days/yr for $\Delta_t CO_2$ DZCP. The $\Delta_t CO_2$ DZCP is very sensitive to the curve we use to perturb the time series due to the relatively flat period of near-zero flux during the dormant period preceding it (it does not take much to bring this below zero). While for the synthetic example, we have used a smoothed version of the BRW time series, in practice there is substantial variability in the spring shoulder so that it is often difficult to accurately define a trend in the $\Delta_t CO_2$ DZCP. To address this we use an operational definition that is defined as 25% from zero to the PU, which in this case has a trend of 0.35 days/yr. The $\Delta_t CO_2$ metrics were found to be better at capturing the springtime trend to within 23% and 16% respectively, than the equivalent CO_2 mole fraction metric that underestimates the trend by 63% with implications for using this metric to interpret changes in phase. There is little change in any of the UZCP metrics (typically <0.025 days/yr) as a result of aliasing. The wavelet detrending introduces a -0.01%/yr trend in peak CO_2 uptake and a concurrent increase in peak CO_2 release of 0.14%/yr corresponding to -0.4% and 5.6% across the 40 year time series respectively. This is considered an aliasing error when interpreting the real data in the main paper and is relatively small considering the large trends introduced in spring uptake.

Figure 13 shows the same calculation but for introducing an earlier autumn onset of net CO_2 release of 0.30 days/yr. We find that the metrics for spring phase respond to the prescribed change in autumn phase due to aliasing, where the mole fraction and $\Delta_t CO_2$=0 metrics had non-zero trends up to ~-0.16 days/yr. All three UZCP phase metrics underestimate the change in the defined phase change by amounts ranging from 11–22% where the CO_2 UZCP performed the best. The earlier onset of net CO_2 release aliases into a 2.5% decrease in peak CO_2 release and a 5% increase in peak CO_2 across the entire time series.

Perturbing the magnitude of net uptake and release of CO_2

Figure 14 shows the results of introducing a progressive enhancement of CO_2 uptake of roughly 0.70% yr^{-1}, equivelant to a 28% increase over 40 years. We introduce the trend by multiplying the

negative flux by an increasing amount each year, which does not have an effect on timing of net CO_2 uptake or release. We also introduce two exceptional years to emulate the effect of interannual variability such as that driven by climate phenomena like ENSO.

We find that the wavelet transform attributes the 0.70%/yr increased uptake as 0.59%/yr uptake and 0.20%/yr release. The mole fraction metrics infer non-zero UZCP and DZCP phase changes of 0.06 days/yr and 0.16 days/yr, respectively, while the 25% $\Delta_t CO_2$ UZCP and DZCP metrics, our operational metrics, exhibits negligible trends as expected. The exceptional years are captured in the PU and PR metrics, while the CO_2 UZCP is the most affected out of the phase metrics. In addition, information from the exceptional years of uptake is aliased into the CO_2 UZCP and is spread over a number of years rather than just one. This is not the case for the $\Delta_t CO_2$ metrics indicating that they are better for estimating interannual variability.

Simultaneous variations in phase and peak uptake and release

Figure 15 shows the results from a final experiment that describes a calculation in which we simultaneously perturb the phase of the spring and autumn, as diagnosed by the $\Delta_t CO_2=0$, and the PU and PR. We also superimpose gaussian random noise within ± 10 days and $\pm 25\%$ to describe year-to-year changes to the phase and to the PU and PR, respectively.

Despite large interannual variability, there is a negligible trend in the spring timing of CO_2 uptake (-0.02 days/yr) which is captured by the $\Delta_t CO_2$ phase metric (0.02 days/yr). The CO_2 DZCP trend has the opposite sign and additionally overestimates the magnitude of the trend by a factor of four. The trend in the autumn $\Delta_t CO_2$ phase metric (0.05 days/yr) underestimates the expected trend (0.09 days/yr) by ∼45%, while the CO_2 UZCP overestimates it by a factor of 2.8. The estimated trend in PU is 0.54% yr which is 80% of the expected trend (0.68% yr), while the estimated PR trend (0.14% yr) is opposite in sign and double the magnitude of the expected trend (-0.07%). The estimated CUP trend is positive but roughly zero, which is a little smaller than the expected trend of 0.12 days/yr. The increase in PU (which is a factor of three larger than the rise in PR) and the roughly zero trend estimated for the CUP hints at a probable increase in annually integrated net uptake. The trend in net flux in this example is indeed negative with an increase in uptake of -0.16ppm CO_2/yr.

We find that the analysis of synthetic time series indicates that $\Delta_t CO_2$ metrics can reproduce prescribed phase changes to within 30%, but trends with a magnitude of <0.1 days/yr were uncertain in magnitude and sign. Strong shifts in spring and autumn phase caused changes in PU and PR of <6% due to aliasing. Strong trends in PU and PR were estimated to within 25%. Estimates of changes in PU, PR and CUP were used to estimate whether net increases in uptake or release were taking place.

13

B3 Monte Carlo simulations

We used a Monte Carlo Simulation (MCS) to study the ability of the wavelet transform to simultaneously determine the PU, PR and changes in phase. We generated a thousand synthetic time series with random trends and variability such as the one illustrated in Figure 15, where Figure 16 shows the probability distributions of the trends introduced in the net carbon fluxes and changes in the CUP. Integrated uptake and release of carbon was in the range of -0.25 to 0.25 ppm/yr, while changes in the phase were within 1 day/yr. We then regressed the expected trends in phase, PU and PR against the values we estimated using our analysis. The regression coefficient was used as an estimate of the mean bias, while the Pearson correlation coefficient r is indicative of consistency in the bias and the likelihood of the estimates to deviate far from the expected value.

Figure 17 shows some of the results from the MCS regression analysis where we compare expected and estimated trends. The figure also shows estimates where we detected the wrong sign of the trend and the quantity of statistically significant trends ($p < 0.05$) that were and were not detected in the analysis. The results of the MCS indicated a large mean negative bias in the CO_2 DZCP trend (-0.57±4%), but also a large spread about the mean bias that suggests that the CO_2 DZCP is more susceptible to aliasing. On the other hand, the use of $\Delta_t CO_2$=25% PU resulted in a relatively small mean bias (-14±2%) with high consistency (r^2=0.94). Although the mean bias was less in the MCS for the CO_2 UZCP (-1±3%), it was less consistent (r^2=0.80). The $\Delta_t CO_2$ UZCP had a mean bias of -23±1% (r^2=0.97). Differences between the spring and autumn phase biases calculated from CO_2 and $\Delta_t CO_2$ phase metrics carry through to the respective CUP estimates, where the $\Delta_t CO_2$ CUP had a mean bias of -28±1% (r^2=0.93) relative to a bias of -55±1% (r^2=0.45) in the CO_2 CUP. Estimates of $\Delta_t CO_2$ phase metrics tended to be more consistent, and while it resulted in significantly more accurate estimates of the trend in spring phase, the autumn phase was better represented by the CO_2 UZCP. We expect that this is a result of the asymmetry of the high latitude CO_2 seasonal cycle. Analysis of peak rates of uptake and release resulted in mean biases of -18±2% and -28±2% for PU and PR respectively. In general, the trend estimates from the analysis had the correct sign so long as the trend was sufficiently large (>0.25%/yr for PU and PR, and >0.1 days/yr for changes in phase). The CO_2 phase metric trend estimates were the most likely to have the wrong sign compared to the $\Delta_t CO_2$ phase metrics by 4.5, 4 and 1.5× for the DZCP, UZCP and CUP respectively. Finally, the $\Delta_t CO_2$ metrics were far more effective at detecting statistically significant trends where the CO_2 metrics typically missed 33–50% of them.

Figure 18 shows a regression of the linear trend in integrated CO_2 uptake and release against the estimated seasonal amplitude from the individual MCS runs. We find that the linear trends in annually integrated CO_2 uptake (ppm/yr^2) are correlated with the amplitude trend (ppm/yr). Previous work has shown this is due to the rapid temporal variation in CO_2 associated with the uptake than the release outside of the growing period (Graven et al., 2013).

Appendix C   Analysis of other sites

Table 3 summarises the analysis of all the high northern latitude stations we have considered in this study.

Appendix D   Analysis of ancillary data

D1   Surface temperature and NDVI

Table 4 shows that mean surface land temperature has warmed significantly at high-latitudes since 1970. We define a thermal growing season (TGS) with a threshold temperature of 5°C, the minimal temperature typically required for the onset of photosynthesis, following Barichivich et al. (2012). We find that an earlier onset of the mean temperature reaching 5°C in spring, TGS_{BEG}, and a delay in the temperature dropping below 5°C in autumn, TGS_{END}, results in a significant lengthening of the thermal growing season, TGS_{LEN} since 1970 for a number of high latitude regions. Of the Transcom regions, we find that Europe exhibits the largest change in TGS_{LEN} of $\sim 3.41 \pm 0.9$ days/decade, resulting from equal shifts in TGS_{BEG} and TGS_{END}. Europe is followed by roughly equal changes in Boreal North America and Asia, however these regions exhibit different changes in spring and autumn temperature. The largest overall changes are seen $>60°N$ where TGS_{LEN} has increased by up to 5 ± 1.7 days/decade where a larger proportion of this change is due to autumn warming. This increase in TGS_{LEN} suggests that the potential period during which plant growth is not hindered by low temperatures has been significantly extended by approximately 11 days ($>45°N$) and 20 days ($>60°N$) since 1970, consistent with previous findings (Linderholm (2006), Barichivich et al. (2012)). Table D2 shows the relationship between northern high latitude land surface temperature anomalies with the BRW CO_2 and $\Delta_t CO_2$ phase metrics throughout 1973–2012. We find there are significant results depending on whether CO_2 and $\Delta_t CO_2$ phase metrics are used.

The warming-induced earlier onset of springtime carbon uptake is also supported by observed increases in vegetation greenness described by NDVI inferred from space-borne sensors (Gong and Shi, 2003; Mao et al., 2012; Cong et al., 2013). Increases in autumn NDVI have also been observed and while this is indicative of increased photosynthetic activity is not necessarily inconsistent with the observed early onset of net carbon release. This is because it does not provide information about respiration processes. Our analysis of NDVI data (not shown) finds an increases of vegetation greenness in apring and autumn have led to significant lengthening of the photosynthetic growing season over the measurement period, where autumn greening is changing in most regions at a greater rate than spring greening.

15

D2 δ^{13}C data

500 Figure 4 shows δ^{13}C data over CBA, with the corresponding CO_2 mole fraction data. Measurements of δ^{13}C show a strong seasonal variation, which is anti-correlated with CO_2. Plants preferentially take the lighter carbon ^{12}C isotope out of the atmosphere through photosynthesis during spring and summer resulting in an increase in δ^{13}C, and release more ^{12}C than ^{13}C during autumn and winter resulting in a decrease in δ^{13}C.

505 Figure 9 shows a similar phase analysis for $(-1)\times\delta^{13}$C and $(-1)\times\Delta\delta^{13}$C, comparing it with variability and trends with the corresponding CO_2 values. Table D2 shows regression coefficients and mean statistics for the spring and autumn phase and the CUP. We find that atleast 68% of the observed trend in CO_2 DZCP and UZCP can be explained by variations in colocated measurements of δ^{13}C. This suggests that the terrestrial biosphere is largely responsible for observed CO_2 vari-

510 ability with the remainder due to atmospheric transport and other minor source variations. This result is consistent with previous work (Graven et al., 2013) that showed using an atmospheric transport model that atmospheric transport variations contributed <7% of the observed variation in CO_2 seasonal amplitudes at high northern latitudes.

References

Bacastow, R. B., Keeling, C. D., and Whorf, T. P.: Seasonal Amplitude increase in atmospheric CO_2 concentration at Mauna Loa, Hawaii, 1959 - 1982, J. Geophys. Res., 90, 1985.

Ballantyne, A. P., Alden, C. B., Miller, J. B., Tans, P. P., and White, J. W. C.: Increase in observed net carbon dioxide uptake by land and oceans during the past 50 years, Nature, 488, 70–72, 2012.

Barichivich, J., Briffa, K. R., Osborn, T. J., Melvin, T. M., and Caesar, J.: Thermal growing season and timing of biospheric carbon uptake across the Northern Hemisphere, Global Biogeochem. Cycles, 26, 2012.

Barichivich, J., Briffa, K. R., Myneni, R. B. Osborn, T. J., Melvin, T. M., Ciais, P., Piao, L., and Tucker, C.: Large-scale variations in the vegetation growing season and annual cycle of atmospheric CO_2 at high northern latitudes from 1950 to 2011, Glob. Change Biol., 19, 3167–3183, 2013.

Cong, N., Wang, T., Nan, H., Ma, Y., Wang, X., Myneni, R. B., and Piao, S.: Changes in satellite-derived spring vegetation green-up date and its linkage to climate in China from 1982 to 2010: a multimethod analysis, Glob. Change Biol., 19, 881–891, 2013.

Dlugokencky, E., Lang, P. M., Crotwell, A. M., Masarie, K. A., and Crotwell, M. J.: Atmospheric Methane Dry Air Mole Fractions from the NOAA ESRL Carbon Cycle Cooperative Global Air Sampling Network, 1983–2013, Tech. rep., NOAA, 2014.

Gloor, M., Sarmiento, J. L., and Gruber, N.: What can be learner about carbon cycle climate feedbacks from the CO_2 airborne fraction?, Atmos. Chem. Phys., 10, 7739–7751, 2010.

Gong, D.-Y. and Shi, P.-J.: Northern hemispheric NDVI variations associated with large-scale climate indices in spring, Int. J. Remote Sensing, 24, 2559–2566, 2003.

Graven, H. D., Keeling, R. F., Piper, S. C., Patra, P. K., Stephens, B. B., Wofsy, S. C., Welp, L. R., Sweeney, C., Tans, P. P., Kelley, J. J., Daube, B. C., Kort, E. A., Santoni, G. W., and Bent, J. D.: Enhanced Seasonal Exchange of CO_2 by Northern Ecosystems Since 1960, Science, 341, 1085–1089, 2013.

Harris, I., Jones, P. D., Osborn, T. J., and Lister, D. H.: Updated high-resolution grids of monthly climatic observations - the CRU TS3.10 Dataset, Int. J. Climatol., Doi: 10.1002/joc.3711, 2013.

Kaufmann, R. K., Paletta, L. F., Tian, H. Q., Myneni, R. B., and D'Arrigo, R. D.: The Power of Monitoring Stations and a CO_2 Fertilization Effect: Evidence from Causal Relationships between NDVI and Carbon Dioxide, Earth Interactions, 12, 2008.

Keeling, C. D., Chin, J. F. S., and Whorf, T. P.: Increased activity of northern vegetation inferred from atmospheric CO_2 measurements, Nature, 382, 146–149, 1996.

Lim, C., Kafatos, M., and Megonigal, P.: Correlation between atmospheric CO_2 concentration and vegetation greenness in North America: CO_2 fertilization effect, Clim. Res., 28, 11–22, 2004.

Linderholm, H. W.: Growing season changes in the last century, Agric. For. Meteorol., 137, 1–14, 2006.

Los, S. O.: Analysis of trends in fused AVHRR and MODIS NDVI data for 1982-2006: Indication for a CO_2 fertilization effect in global vegetation, Global Biogeochem. Cycles, 27, 1–13, 2013.

Mao, J., Shi, X., Thornton, P. E., Piao, S., and Wang, X.: Causes of spring vegetation growth trends in the northern mid-high latitudes from 1982 to 2004, Environ. Res., 7, 2012.

Piao, S., Ciais, P., Friedlingstein, P., Peylin, P., Reichstein, M., Luyssaert, S., Margolis, H., Fang, J., Barr, A., Chen, A., Grelle, A., Hollinger, D. Y., Laurila, T., Lindroth, A., Richardson, A. D., and Vesale, T.: Net carbon dioxide losses of northern ecosystems in response to autumn warming, Nature, 451, 49–52, 2008.

17

Pinzon, J., Brown, M. E., and Tucker, C. J.: Satellite time series correction of orbital drift artifacts using empirical mode decomposition, Hilbert-Huang Transform: Introduction and Applications, pp. 167–186, 2005.

Suntharalingam, P., Randerson, J. T., Krakauer, N., Logan, J. A., and Jacob, D. J.: The influence of reduced carbon emissions and oxidation on the distribution of atmospheric CO_2: implications for inversion analysis,

565   Global Biogeochem. Cy., 19, 2005.

Thompson, M. L., Enting, I. G., Pearman, G. I., and Hyson, P.: Interannual variation of atmospheric CO_2 concentration, J. Atmos. Chem., 4, 125–155, 1986.

Thompson, R.: The relationship of the phase and amplitude of the annual cycle of CO_2 to phenological events, Plant Ecolog. Divers., 4, 2011.

570   Thompson, R. and Clark, R. M.: Is spring starting earlier?, The Holocene, 18,1, 2008.

Torrence, C. and Compo, G. P.: A Practical Guide to Wavelet Analysis, Bull. Am. Meteorol. Soc., 79, 1998.

Tucker, C. J., Pinzon, J. E., Brown, M. E., Slayback, D., Pak, E. W., Mahoney, R., Vermote, E., and Saleous, N.: An Extended AVHRR 8-km NDVI Data Set Compatible with MODIS and SPOT Vegetation NDVI Data, Int. J. Remote Sens., 26(20), 4485–4498, 2005.

575   Zhao, C. L. and Tans, P. P.: Estimating uncertainty of the WMO mole fraction scale for carbon dioxide in air, J. Geophys. Res., 111, 2006.

Table 1. Parameters used by the control wavelet transform for monthly and weekly spectral decomposition of CO_2 mole fraction.

Parameter	$\delta t=1/12$	$\delta t=1/52$
δj	0.25	0.01
s_0	$2\delta t$	δt
C_δ	0.7784	0.7784
ψ_0	$\pi^{-\frac{1}{4}}$	$\pi^{-\frac{1}{4}}$

Table 2. Global decadal mean growth rates (ppm/yr) and the corresponding growth rate due to fossil fuel combustion.

Decade	No. Stations	Fossil Fuel (FF)	Growth Rate (GR)	GR 1σ	GR - FF
1960-1969	1	1.51	0.86	N/A	-0.65
1970-1979	2	2.25	1.21	0.055	-1.04
1980-1989	13	2.61	1.58	0.108	-1.03
1990-1999	38	3.02	1.48	0.056	-1.54
2000-2009	49	3.79	1.90	0.076	-1.89

Site Info		Spring Phase				Autumn Phase				Uptake Period		C. Exchange		
Site	Times-pan	CO_2 DZCP (days/yr)	$\Delta_t CO_2$ DZCP (days/yr)	$\Delta_t CO_2$ = 25% PU (days/yr)	$\Delta_t CO_2$ = PU (days/yr)	CO_2 UZCP (days/yr)	$\Delta_t CO_2$ UZCP (days/yr)	$\Delta_t CO_2$ = 25% PR (days/yr)	$\Delta_t CO_2$ = PR (days/yr)	CO_2 CUP (days/yr)	$\Delta_t CO_2$ CUP (days/yr)	Seas. Amp. (ppm/yr)	PU (%/yr)	PR (%/yr)
ALT	1986-2013	-0.14 ±0.15 (p<0.1)	-0.34 ±0.83 (p>0.1)	-0.16 ±0.26 (p>0.1)	-0.18 ±0.26 (p>0.1)	-0.27 ±0.19 (p<0.01)	-0.10 ±0.17 (p>0.1)	-0.09 ±0.20 (p>0.1)	0.15 ±0.59 (p>0.1)	-0.02 ±0.20 (p>0.1)	0.05 ±0.32 (p>0.1)	0.10 ±0.04 (p<0.01)	0.61 ±0.60 (p<0.01)	0.40 ±0.60 (p<0.1)
BRW	1973-2013	-0.20 ±0.08 (p<0.01)	-0.02 ±0.47 (p>0.1)	-0.14 ±0.14 (p<0.05)	-0.21 ±0.15 (p<0.01)	-0.18 ±0.14 (p<0.05)	-0.25 ±0.08 (p<0.01)	-0.26 ±0.10 (p<0.01)	-0.25 ±0.10 (p<0.1)	0.02 ±0.15 (p>0.1)	-0.11 ±0.16 (p>0.1)	0.09 ±0.02 (p<0.01)	0.65 ±0.34 (p<0.01)	0.42 ±0.34 (p<0.05)
CBA	1979-2012	-0.14 ±0.15 (p<0.1)	-0.56 ±0.34 (p<0.01)	0.06 ±0.11 (p>0.1)	-0.24 ±0.37 (p>0.1)	-0.27 ±0.27 (p<0.05)	-0.16 ±0.17 (p<0.1)	-0.17 ±0.20 (p<0.1)	0.14 ±0.33 (p>0.1)	-0.07 ±0.29 (p>0.1)	-0.22 ±0.34 (p>0.1)	0.07 ±0.04 (p<0.01)	0.66 ±0.48 (p<0.01)	0.58 ±0.48 (p<0.05)
ICE	1993-2013	0.34 ±0.27 (p<0.05)	0.62 ±0.98 (p<0.01)	0.63 ±0.65 (p<0.01)	0.25 ±0.54 (p<0.1)	-0.13 ±0.28 (p>0.1)	0.18 ±0.25 (p>0.1)	0.22 ±0.24 (p<0.1)	0.11 ±0.99 (p>0.1)	-0.21 ±0.33 (p>0.1)	-0.45 ±0.64 (p>0.1)	0.06 ±0.04 (p<0.01)	0.97 ±0.94 (p<0.01)	0.92 ±0.92 (p<0.05)
SHM	1987-2012	-0.40 ±0.18 (p<0.01)	-0.59 ±0.45 (p<0.05)	-0.45 ±0.34 (p<0.05)	-0.54 ±0.40 (p<0.01)	-0.27 ±0.22 (p<0.05)	-0.13 ±0.23 (p>0.1)	-0.11 ±0.25 (p>0.1)	-0.15 ±0.33 (p>0.1)	-0.13 ±0.24 (p>0.1)	0.32 ±0.44 (p>0.1)	0.06 ±0.05 (p<0.05)	-0.24 ±0.75 (p>0.1)	-0.05 ±0.69 (p>0.1)
STM	1981-2010	-0.17 ±0.14 (p<0.05)	-0.60 ±0.74 (p>0.1)	-0.03 ±0.65 (p>0.1)	-0.04 ±0.27 (p>0.1)	-0.24 ±0.25 (p<0.1)	-0.01 ±0.15 (p>0.1)	-0.01 ±0.18 (p>0.1)	0.16 ±0.62 (p>0.1)	-0.07 ±0.31 (p>0.1)	0.02 ±0.66 (p>0.1)	0.05 ±0.03 (p<0.01)	0.04 ±0.63 (p>0.1)	0.72 ±0.62 (p<0.05)
ZEP	1994-2013	-0.01 ±0.21 (p>0.1)	-1.24 ±1.78 (p>0.1)	0.01 ±0.61 (p>0.1)	-0.06 ±0.40 (p>0.1)	0.40 ±0.52 (p>0.1)	-0.16 ±0.33 (p>0.1)	-0.24 ±0.38 (p>0.1)	0.43 ±1.20 (p>0.1)	0.12 ±0.25 (p>0.1)	-0.18 ±0.76 (p>0.1)	0.14 ±0.05 (p<0.01)	1.00 ±1.06 (p<0.05)	-0.30 ±1.07 (p>0.1)

Table 3. Estimated trends of downward and upward zero crossing points (DZCP and UZCP, respectively), peak uptake and release (PU and PR, respectively), and carbon uptake period (CUP) calculated from CO_2 and $\Delta_t CO_2$ data for seven high latitude measurement sites (Figure 1). The 95% confidence intervals and p-values are calculated for each trend estimate.

Table 4. Temperature Linear Trend Analysis (1970-2011) for the beginning and end of the thermal growing season.

	$\mathbf{TGS}_{BEG}$ (Days Decade^{-1})				Spring T ($^{\circ}$C Decade^{-1})			
Region	Trend	unc	r^2	p-value	Trend	unc	r^2	p-value
ASBor	-1.39	±0.49	0.45	<0.01	0.58	0.27	0.32	p<0.01
Europe	-1.67	±0.52	0.51	<0.01	0.33	0.11	0.47	p<0.01
USBor	-1.06	±0.72	0.18	<0.01	0.34	0.25	0.15	p<0.05
>45° N	-1.24	±0.44	0.44	<0.01	0.41	0.13	0.49	p<0.01
>60° N	-2.12	±0.75	0.45	<0.01	0.45	0.18	0.40	p<0.01
	$\mathbf{TGS}_{END}$				Autumn T			
Region	Trend	unc	r^2	p-value				
ASBor	1.07	±0.79	0.16	<0.01	0.57	0.29	0.28	p<0.01
Europe	1.74	±0.66	0.42	<0.01	0.38	0.12	0.49	p<0.01
USBor	1.57	±0.69	0.35	<0.01	0.47	0.21	0.34	p<0.01
>45° N	1.34	±0.47	0.45	<0.01	0.44	0.13	0.55	p<0.01
>60° N	2.85	±1.04	0.43	<0.01	0.52	0.16	0.53	p<0.01
	$\mathbf{TGS}_{LEN}$				Annual T			
Region	Trend	unc	r^2	p-value				
ASBor	2.46	±1.08	0.35	<0.01	0.45	0.16	0.45	p<0.01
Europe	3.41	±0.90	0.60	<0.01	0.35	0.10	0.61	p<0.01
USBor	2.63	±1.25	0.31	<0.01	0.43	0.16	0.41	p<0.01
>45° N	2.57	±0.78	0.52	<0.01	0.40	0.10	0.67	p<0.01
>60° N	4.97	±1.69	0.47	<0.01	0.43	0.11	0.63	p<0.01

CO$_2$			
	DZCP vs. TGS$_{BEG}$	**UZCP vs. TGS$_{END}$**	**CUP vs. TGS$_{LEN}$**
>45°N	1.02±0.47	-0.13±0.73	0.31±0.44
	(r^2=0.34, p<0.01)	(r^2=0.01, p>0.1)	(r^2=0.04, p>0.1)
>60°N	0.63±0.27	-0.11±0.34	0.14±0.22
	(r^2=0.38, p<0.01)	(r^2=0.01, p>0.1)	(r^2=0.04, p>0.1)
Δ_tCO$_2$			
	DZCP vs. TGS$_{BEG}$	**UZCP vs. TGS$_{END}$**	**CUP vs. TGS$_{LEN}$**
>45°N	0.57±0.81	-0.89±0.51	-0.42±0.48
	(r^2=0.05, p>0.1)	(r^2=0.25, p<0.01)	(r^2=0.08, p<0.1)
>60°N	0.28±0.48	-0.42±0.24	-0.19±0.24
	(r^2=0.04, p>0.1)	(r^2=0.26, p<0.01)	(r^2=0.07, p<0.1)

Table 5. Linear regression coefficients that describe the relationship between changes in CO$_2$, Δ_tCO$_2$ and temperature phase metrics at different latitude bands in the high northern latitudes (1973-2012).

	DZCP	**UZCP**	**CUP**
CO$_2$ vs. δ^{13}C	0.94±0.19 (r^2=0.84, p<0.01)	0.59±0.34 (r^2=0.38, p<0.01)	0.60±0.37 (r^2=0.34, p<0.01)
Δ_tCO$_2$ vs. $\Delta\delta^{13}$C	0.68±0.37 (r^2=0.41, p<0.01)	0.95±0.29 (r^2=0.70, p<0.01)	0.88±0.42 (r^2=0.48, p<0.01)

Table 6. Linear regression coefficients that describe the relationship between changes in CO$_2$, Δ_tCO$_2$ and δ^{13}C at BRW during the overlapping timespan of the data (1990–2012).
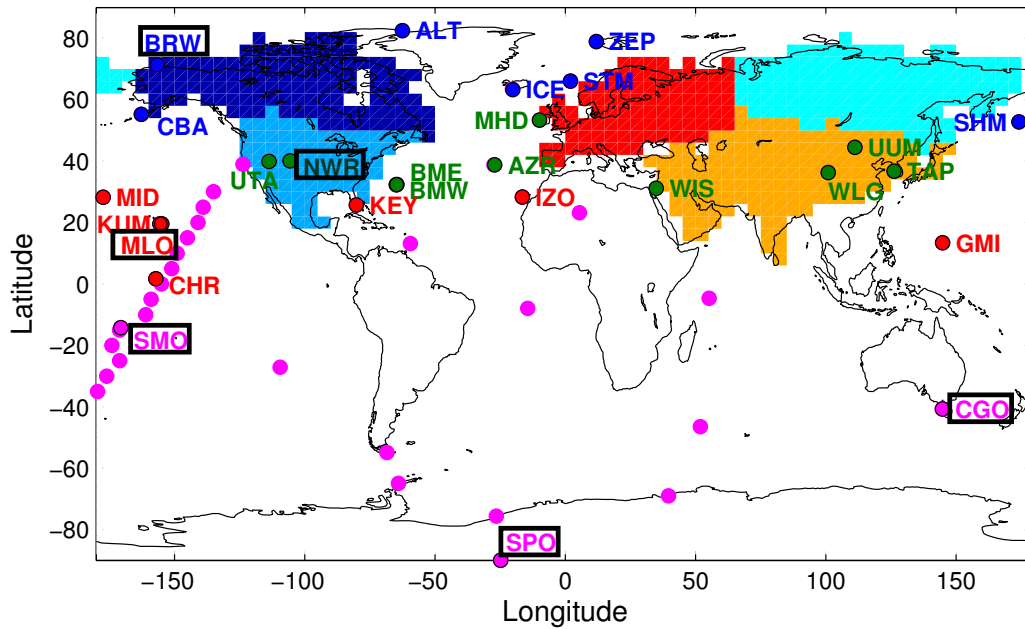
Fig. 1. The NOAA/ESRL stations used in our CO_2 time series analysis. For the seasonal cycle analysis, we split the northern hemisphere stations into three zonal bands, the high, mid and low-latitudes (blue, green and red respectively). The stations shown in magenta are used for growth rate analysis only. The six stations with a black border are those with the longest time series in each $30°$ latitude band. The shaded regions are the temperate and boreal Northern Hemisphere land regions defined in the initial Transcom study, and which we use for analysis of NDVI, temperature, and atmospheric transport.
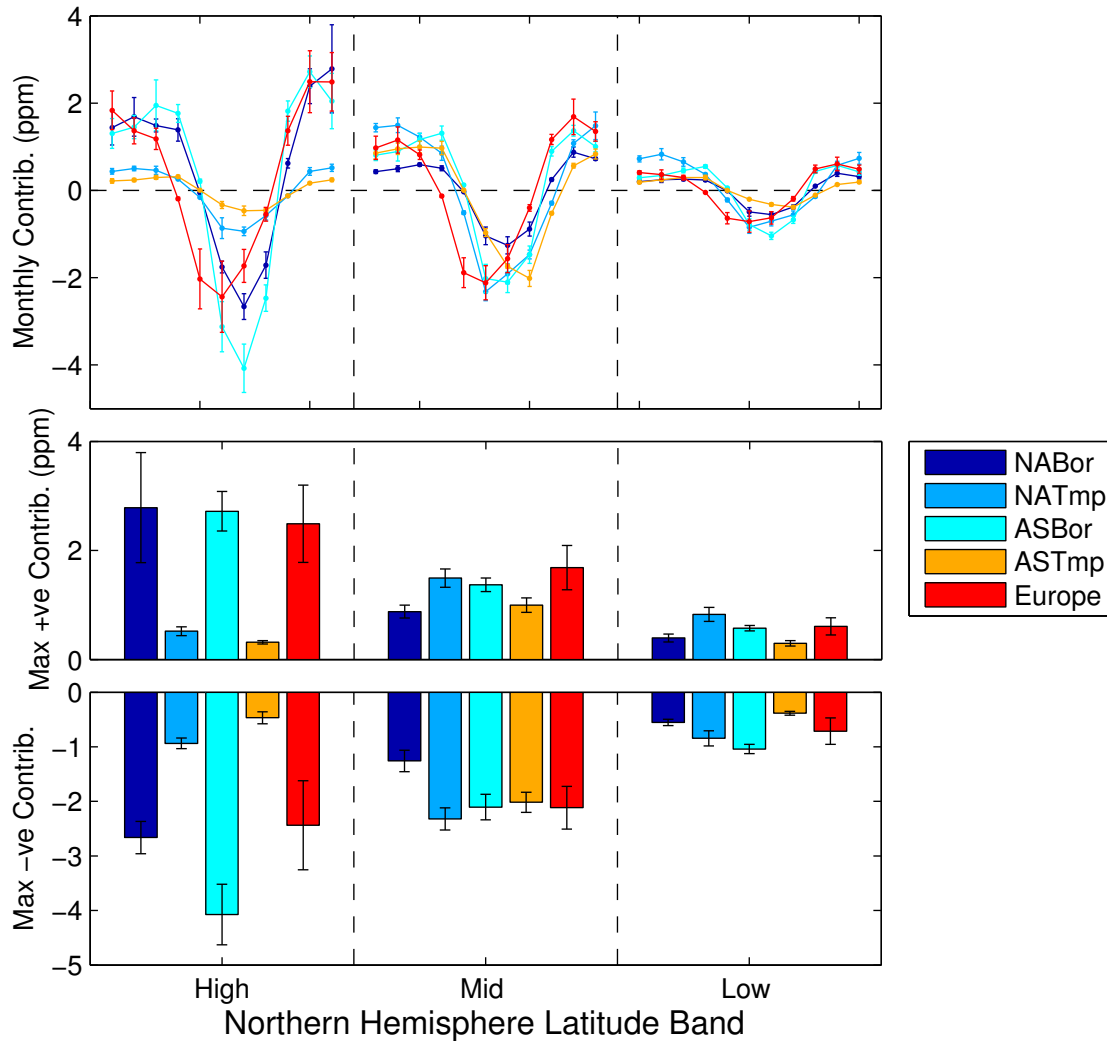
Fig. 2. The maximum CO$_2$ perturbations caused by biosphere carbon fluxes from five Transcom land regions (Figure 1) to the zonal mean concentrations over the high, mid, and low latitude northern hemisphere averaged over 2004–2009. These values were determined by using the GEOS-Chem atmospheric transport model (see main text for further details). The error bars denote the 1σ of the year to year variability over the six-year period. The zonal means are defined as the mean of the gridpoints sampled nearest to the stations shown in Figure 1. Model data from December is missing.
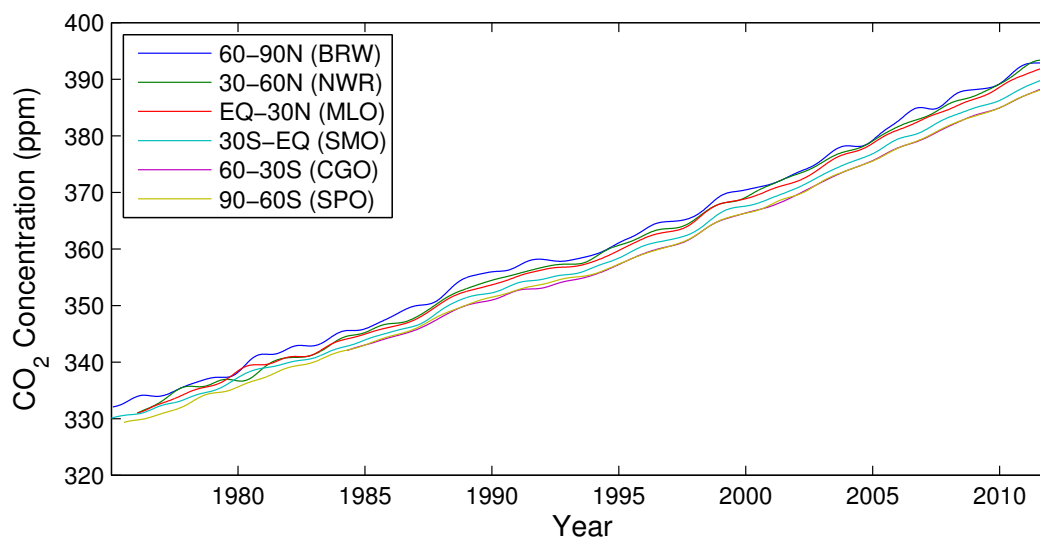
Fig. 3. Reference weekly CO_2 mole fraction measurements (ppm) covering various timespans for $30°$ degree latitude bands used to impute missing data points. BRW, NWR, MLO, SMO, CGO, and SPO are codes to denote Barrow ($71.3°$N, $156.6°$W), Niwot Ridge ($40.0°$N, $105.6°$W), Mauna Loa ($19.5°$N, $155.6°$W), American Samoa ($14.2°$S, $170.5°$W), Cape Grim ($40.7°$S, $144.7°$E), and South Pole ($89.9°$S, $24.8°$W).
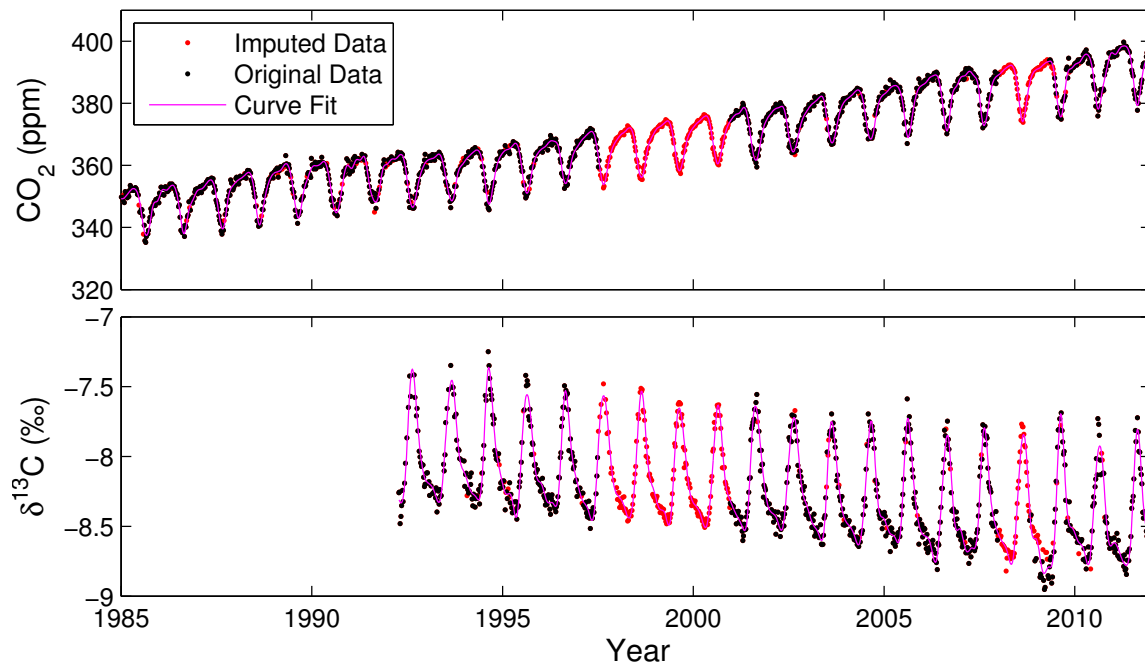
Fig. 4. Weekly (top) CO_2 mole fraction (ppm) measurements (black) and (bottom) $\delta^{13}C$ values (per mil) at Cold Bay, Alaska (CBA, 55.2°N, 162.7°W) from 1980 to 2012. Imputed values, shown in red, are inferred from a locally averaged seasonal cycle adjusted for anomalies in growth rate. Any remaining missing values are extracted from a fitted piecewise cubic spline curve (magenta).
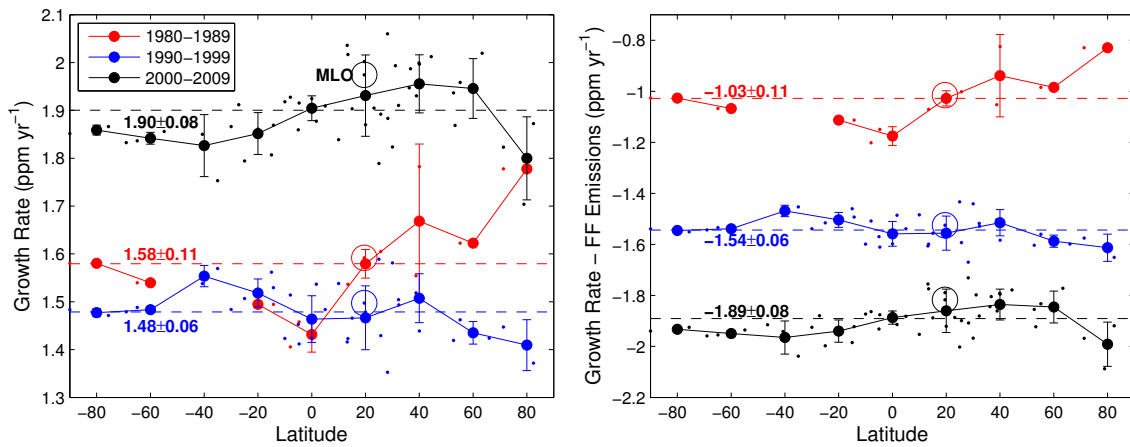
Fig. 5. Decadal mean CO_2 growth rates inferred from individual station measurements and averaged in $20°$ latitude bins having retained (left) and subtracted (right) the decadal mean global fossil fuel emissions (CDIAC). The solid line with error bars represents the decadal mean growth rate in each latitude bin with $\pm 1\sigma$ representing the standard deviation between individual stations in that latitude bin. The global decadal mean growth rate is indicated by the dashed lines and mean values with $\pm 1\sigma$ representing the standard deviation between all stations. Values for MLO, which are typically taken to be representative of the global growth rate are highlighted with a circle. Time series of annual growth rates were determined for individual CO_2 stations before first calculating decadal mean growth rates, and second binning the decadal mean growth rates into $20°$ latitude bins. We subtract a global mean growth rate due to fossil fuel combustion from all stations.
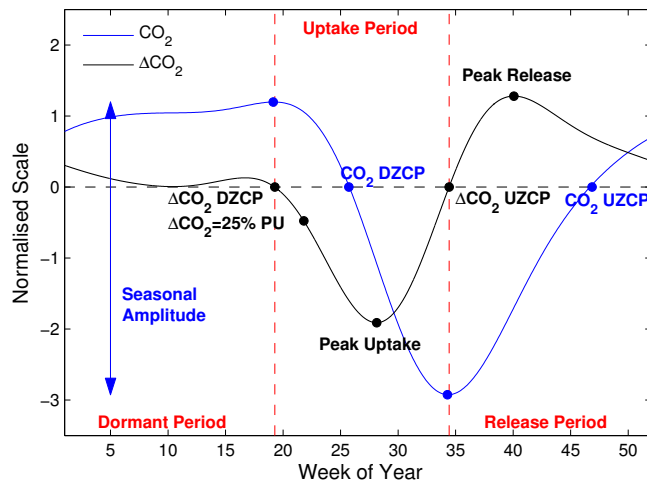
Fig. 6. A schematic describing the metrics we use to characterize changes in the amplitude and phase of atmospheric CO_2 (ppm). In this example we use detrended annual and semi-annual components of CO_2 data from Barrow, Alaska.
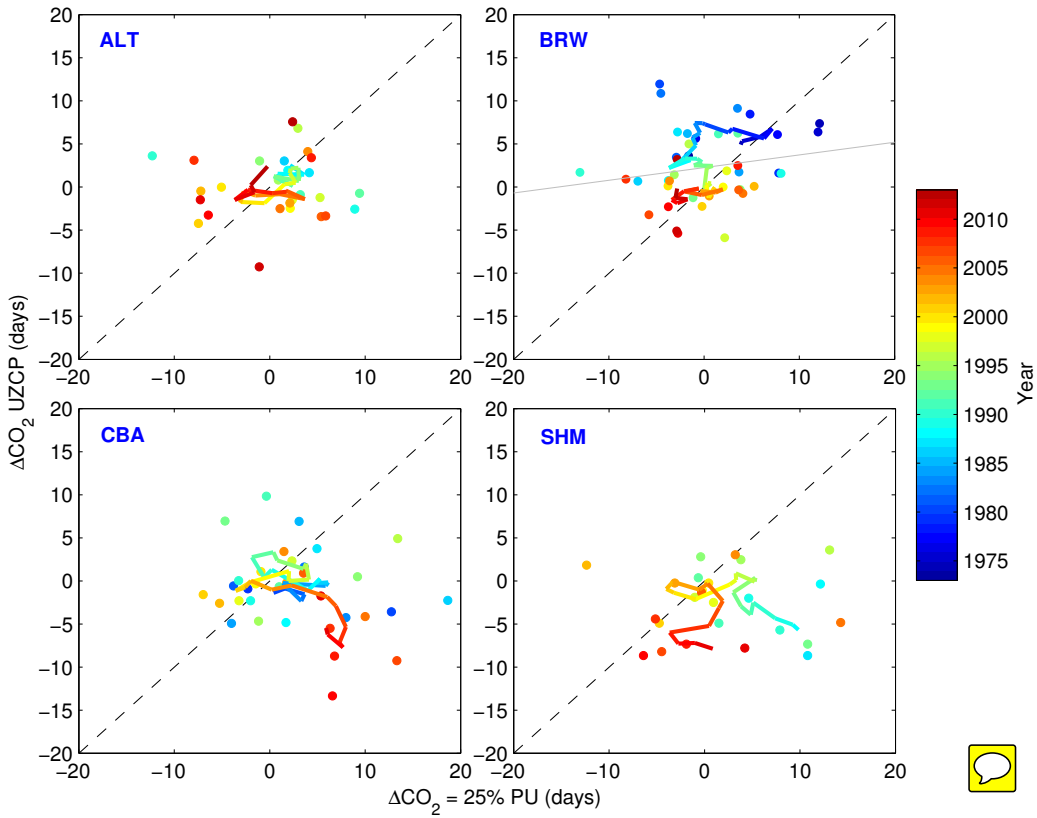
Fig. 7. Scatterplots of the $\Delta_t CO_2$=25% PU (spring phase) and $\Delta_t CO_2$ UZCP (autumn phase) (days) at four high northern latitude sites (see main text). The coloured lines show the trajectory of the 2-year running mean of the scatter plot, where colours represent the year of measurement.
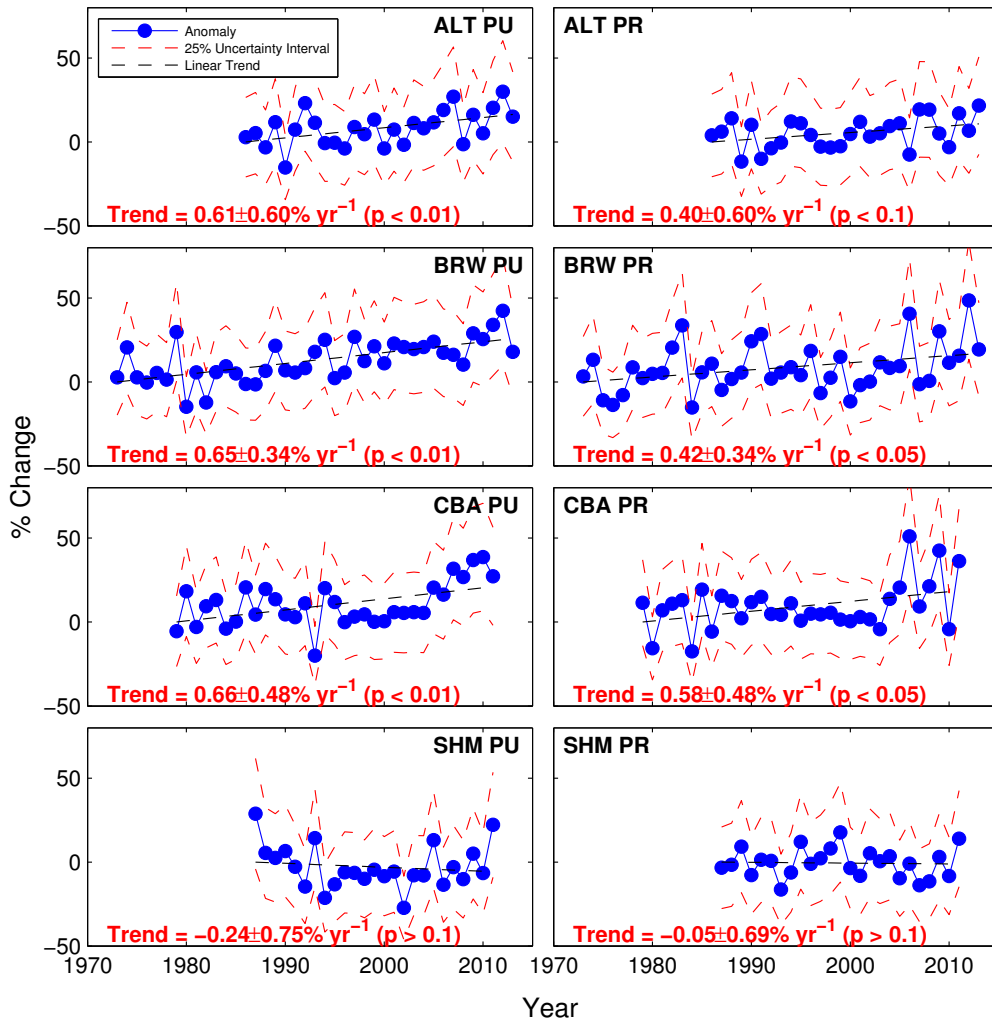
Fig. 8. Time series of the percentage change of peak uptake and release at four high northern latitude sites (see main text). Each panel shows the data as blue closed circles, and the 25% uncertainty interval. The dashed black line is the fitted linear trend that is reported inset of each panel.
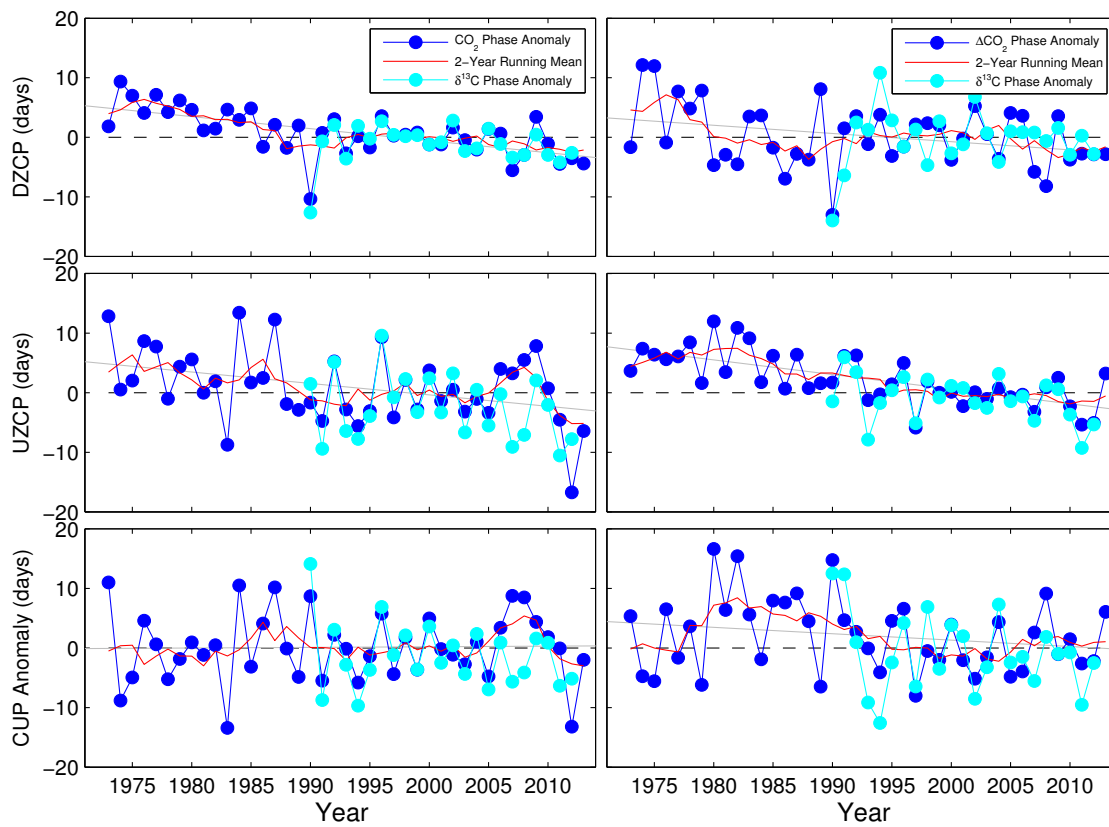
Fig. 9. Time series of phase changes and the corresponding change to the carbon uptake period of $\delta^{13}C$, CO_2, and $\Delta_t CO_2$, expressed as days. The red line is the two-year running mean.

31
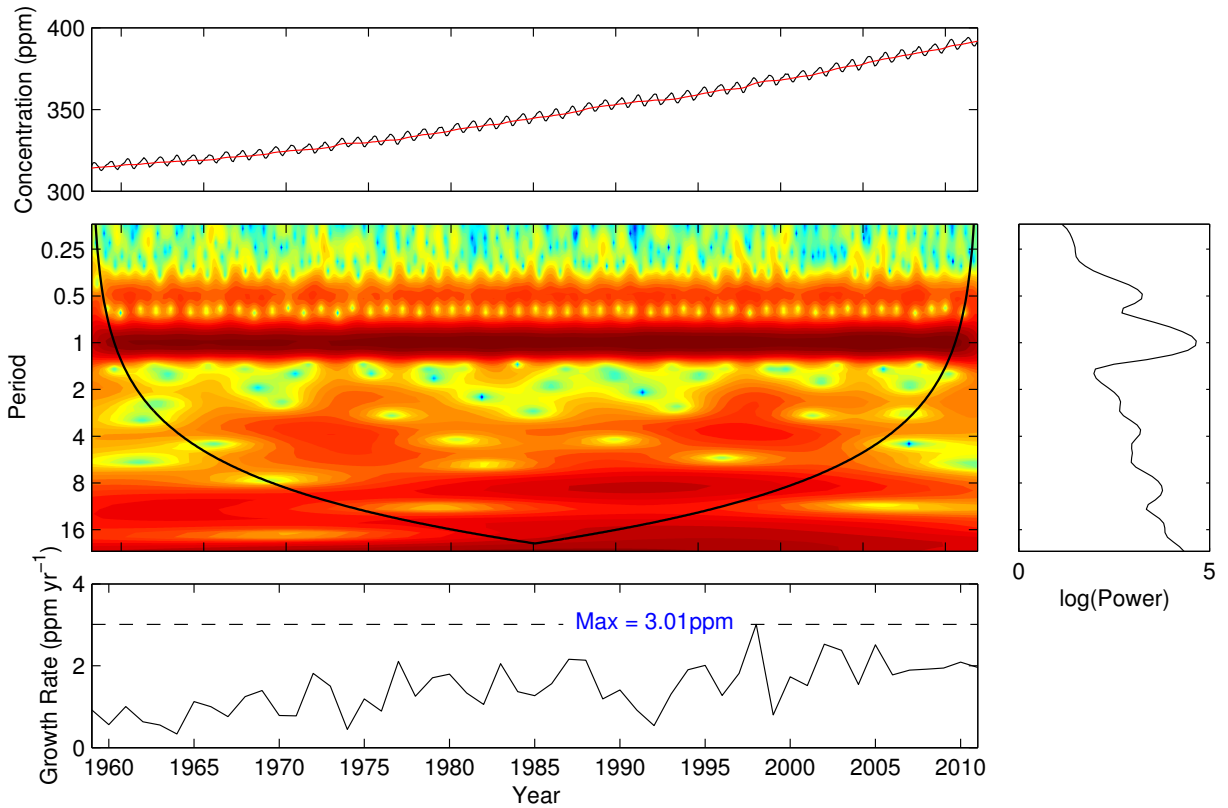
Fig. 10. Top row: weekly mean (black) and low-pass filtered (red, periods >12 months) CO_2 mole fraction time series (ppm) at Mauna Loa, 1959-2012. Middle row: (left) the wavelet power spectrum where the colour scale is $\log$(power). The black solid lines denotes the cone of influence. The power spectrum tends to emphasise very low frequency information so we have subtracted an exponential term prior to applying the wavelet transform to emphasise the high frequency variability (right) the corresponding time-integrated power spectrum. Bottom row: the inferred annual growth rate. of CO_2 (ppm/year).
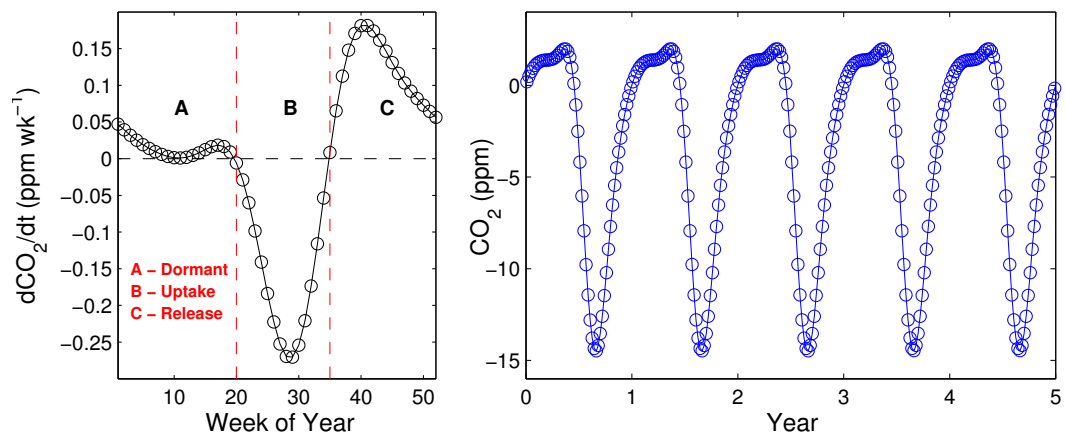
Fig. 11. Synthetic CO_2 "flux" (left), expressed as ppm/week over an annual cycle, and (right) the corresponding mole fraction (ppm) time series repeated over successive years. The CO_2 annual cycle is based on the observed cycle at Barrow Alaska.
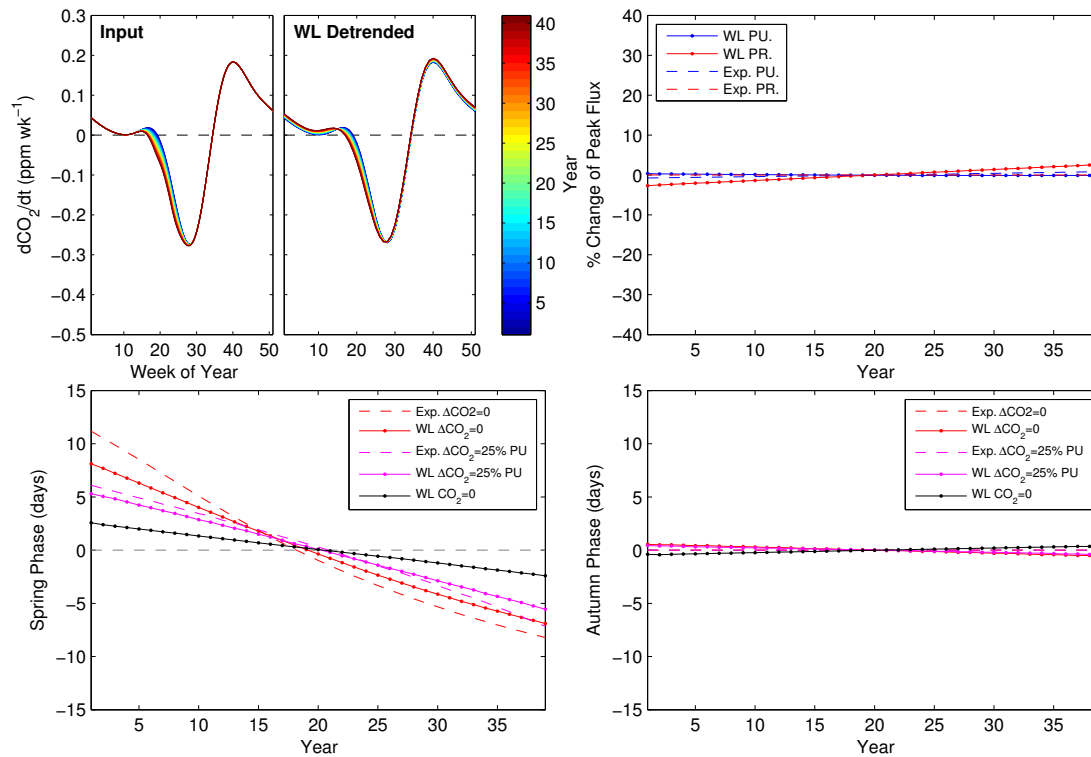
Fig. 12. Wavelet analysis of $\Delta_t CO_2$ flux time series including a prescribed earlier onset of net CO_2 uptake. Top left panel: the defined flux time series and the associated detrended time series. Top right panel: the expected (defined) and actual change in peak uptake and release of CO_2. Bottom panels: the expected (defined) and actual change in (left) DZCP and (right) UZCP, including an operational version of the phase metric as described in the main text.
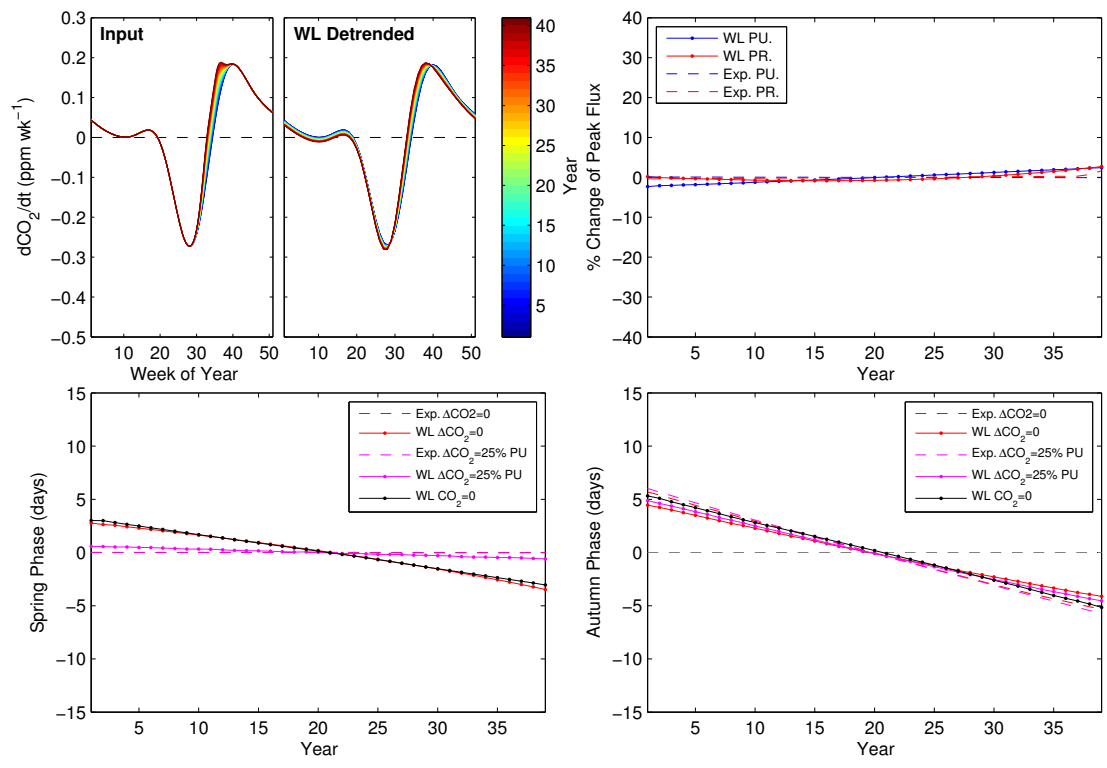
Fig. 13. As Figure 12 but including an earlier autumn onset of net CO_2 release.
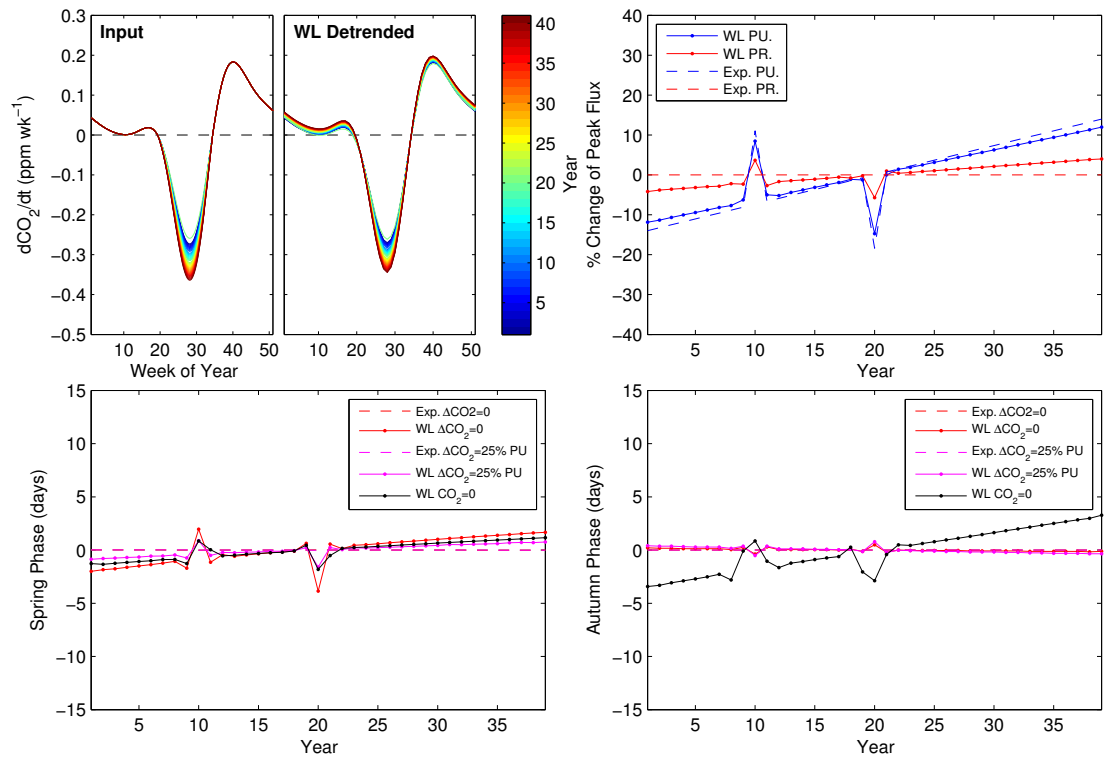
Fig. 14. As Figure 12 but introducing a trend of 0.75%/yr trend in the peak uptake and an anomously high year for uptake and release.
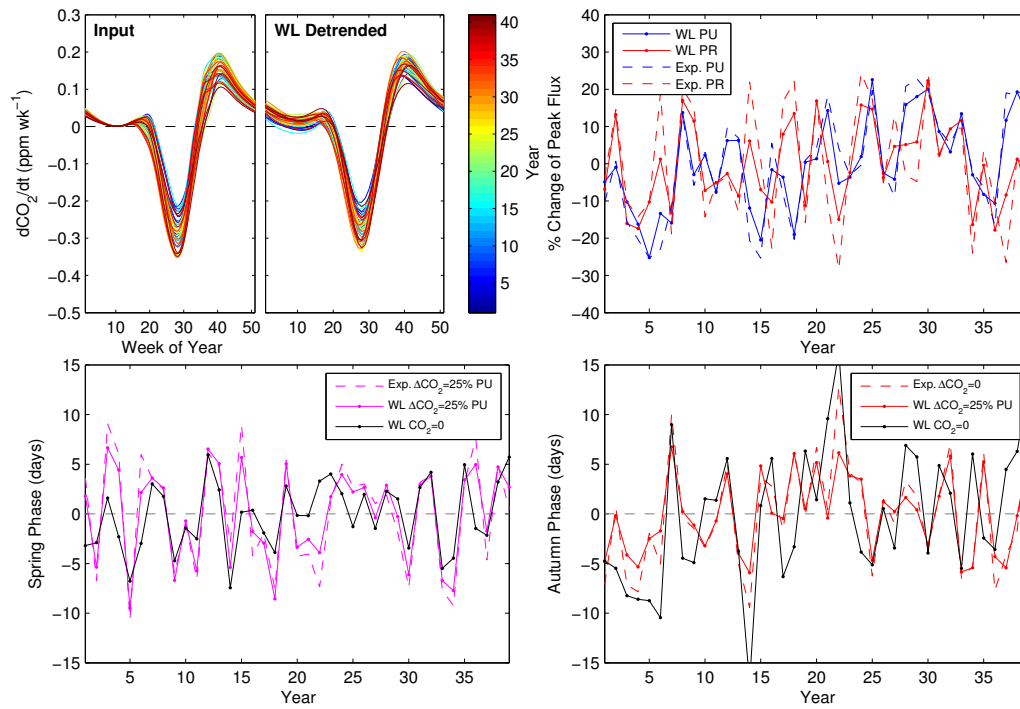
Fig. 15. As Figure 12 but introducing simultaneous trends in spring and autumn phase and in the peak amplitude and release of CO_2. We also superimpose Gaussian random noise to describe interannual variation.
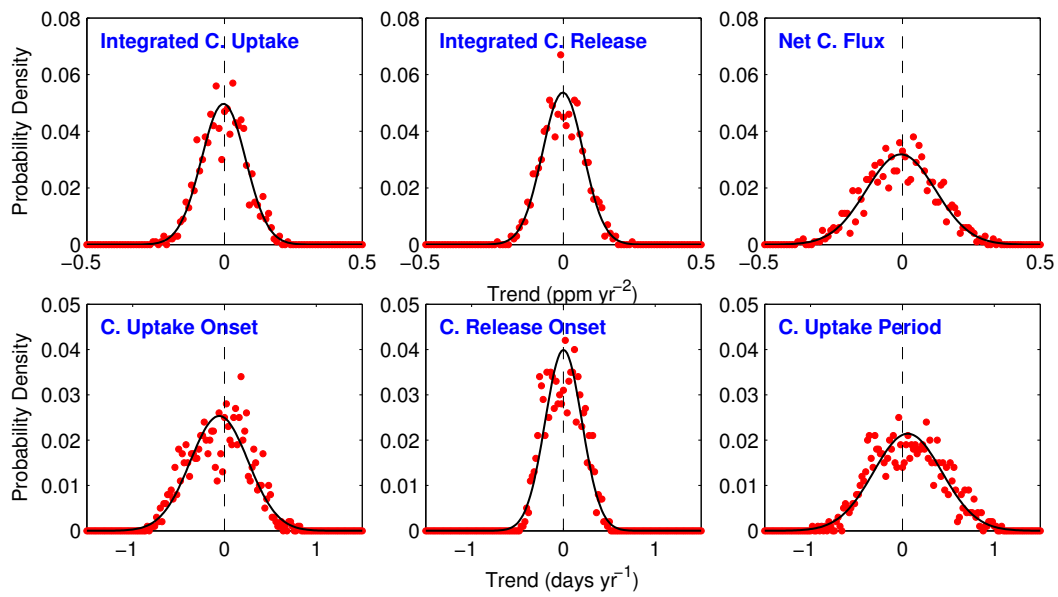
Fig. 16. Probability densities of trends introduced as part of an 1000-member ensemble of synthetic time series generated for the Monte Carlo experiment where the black line is the fitted probability distribution.
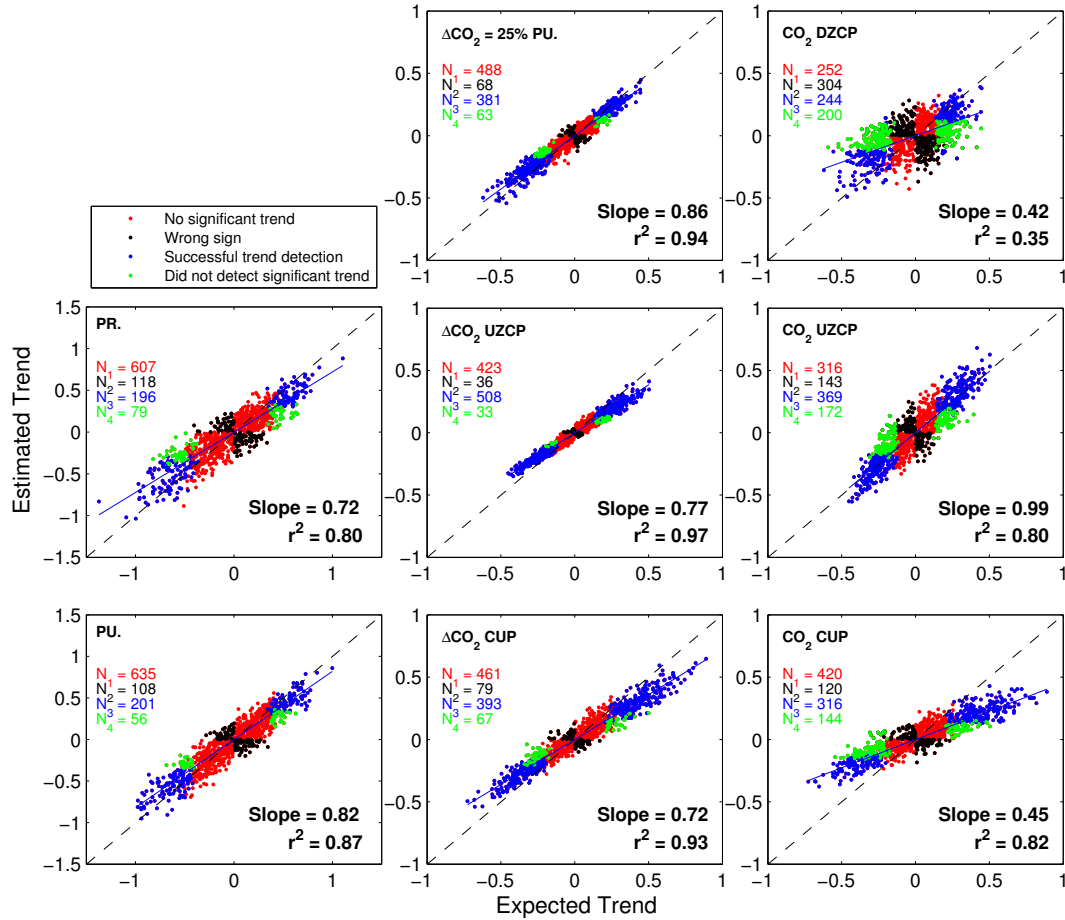
Fig. 17. Regression of expected and estimated linear trends for peak uptake (PU), peak release (PR) and the $\Delta_t CO_2$ and CO_2 phase metrics. Coloured points represent trends there were not (red) statistically significant, (black) trends where we estimated the incorrect sign, (blue) statistically significant trends that were successfully detected, and (green) statistically significant trends that were not detected in the analysis. Statistical significance is at the 5% level. The numbers, $N_{1..n}$ are the number of points in each category and sum to 1000.
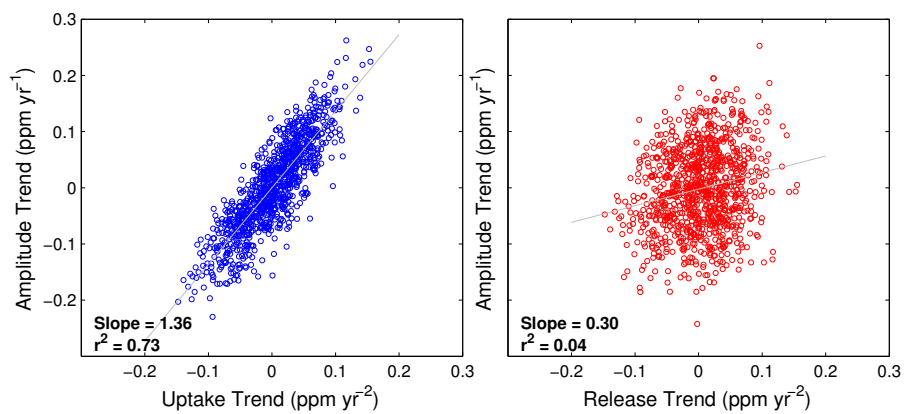
Fig. 18. Scatterplot and associated linear regression coefficients of the amplitude trend (ppm/yr) against the integrated CO_2 uptake and release (ppm/yr^2) from the 1000-member ensemble used in the Monte Carlo experiment.